INVESTIGATION THE EFFECT OF NIKEL AND LITHUIM DOPPING ON THE STRUCTURAL AND OPTICAL PROPERTIES PURE BETA LEAD OXIDE NANOPARTICLES PREPARED BY CO PRECIPITATION TECHNIQUES

A THESIS PRESENTED TO
THE PROGRAM OF GRADUATE STUDIES
ADDIS ABABA UNIVERSITY
IN PARTIAL FULFILLMENT OF THE REQUIREMENTS
FOR THE DEGREE
MASTER OF SCIENCE IN PHYSICS
(Polymer Physics)

By
Berhanu Muluneh

Advisor
Fekadu Gashaw (Professor)

Addis Ababa, Ethiopia

Augest 2024

ADDIS ABABA UNIVERSITY

PROGRAM OF GRADUATE STUDIES

COLLEGE of NATURAL and COMPUTATIONAL SCIENCES

DEPARTMENT OF PHYSICS

This is to certify that the thesis prepared by Berhanu Muluneh under the title: investigate the effect of Ni and Li dopping on the structural and Optical Properties of Pure β- PbO nanoparticles (NPs) Prepared by Co-Pricptation techniques (CPT) for the Degree of Master of Science (M. Sc) in Physics compiles with regulation of the university and meets the accepted standards with respect to originality and quality.

Dated: Augest 2024

Approved by the Examining Committee:

Prof. Fekadu Gashaw **Signature** _____Date____/____/___

Advisor

_____ **Signature** _____Date____/____/___

Examiner

_____ **Signature** _____Date____/____/___

Examiner

ADDIS ABABA UNIVERSITY

Date: **Augest 2024**

Author: **Berhanu Muluneh**

Title: INVESTIGATE THE EFFECT OF Ni AND Li DOPPING ON THE STRUCTURAL AND OPTICAL PROPERTIES PURE BETA LEAD OXIDE NANOPARTICLES PREPARED BY CO PRECIPITATION TECHNIQUES

Department: **Department of Physics**

Degree: **MSc.** Convocation: **Augest** Year: **2024**

Permission is herewith granted to Addis Ababa University to circulate and to have copied for non-commercial purposes, at its discretion, the above title upon the request of individuals or institutions.

Signature of Author

Dedicated to

To my family members for their limitless support, and encouragement

Acknolwledgment

Above all, I thank you to the merciful and almighty God for all he has done in my life that would have been impossible and made me being alive. Secondly my deepest gratitude goes to my advisor Prof. Fekadu Gashaw for his critical comments, constructive suggestion's and advises. Beside I would like to thank you Lemma Tirfe (PhD student at AAU), Alemayehu. And for another AAU Polymer Physics PhD student, my best friends, and my parents for their encouragement and motivation while conducting the study.

Finally, I would like to express my deepest appreciation and love to my parents, brother and sister for their infinite love and support. Simply, there are no words to express my undying admiration

Table of Contents

Contents

List of figures

List of tables

List of Abberviation

Ni	Nikel
Ni: β-pbo	Nikel doped beta lead oxide
CPT	Co-precipitation techniques
EDX/EDS	Energy dispersive x-ray
Eg	Energy gap
eV	Electron volt
FTIR	Fourier Transform Infrared spectroscopy
hr	hours
M	molar
MOCVD	Metal oxide chemical vaporization deposition
MONPs	Metal oxide nanoparticles
NaoH	Sodium hydro oxide
NPs	Nanoparticles
O	Oxides
Pb	Lead
PL	Photoluminescence
SEM	Scanning electron microscopy
Li	Lithium
Li: β-PbO	Lithium doped beta lead oxide
SPT	Spray pyrolysis techniques
TEM	Transmission electron microscopy
UV-Vis	Ultra violet –visible
XRD	X-ray diffraction
β-PbO	Beta lead oxide

Absrtract

The impact of doping pure beta lead oxide (β-PbO) nanoparticles, produced by co-precipitation methods, with nickel (Ni) and lithium (Li) on their optical and structural characteristics. Li doping causes lattice expansion and decreases dislocation density, while Ni doping causes lattice contraction and increases dislocation density, according to structural analysis. Ni doping enhanced and Li doping attenuated the photoluminescence in the 450-550 nm region, according to optical investigations, which showed small changes in band gap energy but considerable fluctuations in photoluminescence intensity. Scanning electron microscopy (SEM) was used to better clarify the morphological effects of the dopants. This study offers significant perspectives on modifying the characteristics of β-PbO nanoparticles for prospective uses in environmental sensing, optoelectronics, and catalysis. Future directions include for creating prototype devices, investigating various synthesis techniques, and working with business to commercialize the results.

Keywords: pure beta Lead oxide, nikel and lithium doping nanoparticles, co-precipitation technique, structural and optical properties

CHAPTER ONE

1. GENERAL INTRODUCTION

1.1 METAL OXIDE NANOPARTICLES (MONPs)

A versatile material with a wide range of scientific and industrial uses is metal oxide nanoparticle (1). Material scientists are still faced with the difficulty of synthesizing high-quality nanoparticles in a cost-effective manner while maintaining chemical purity, phase selectivity, crystallinity, and uniformity in particle size with a regulated state of agglomeration (2). The synthetic process and sensing device technologies pertaining to nanoparticles have garnered significant interest (3).

Recent decades have seen a spectacular expansion in the area of nanotechnology, with metal oxide nanoparticles emerging as an essential class of materials for a wide range of technological applications. These nanoparticles have special qualities that set them apart from their bulk counterparts. Based on the predominant charge carriers, they are categorized as either n-type or p-type. The behavior of n-type and p-type metal oxide nanoparticles in electronic devices is significantly influenced by their charge transport processes and electronic structures, which are different from one another (38).

Because of their high electron mobility and conductivity, N-type metal oxide nanoparticles—which are defined by an abundance of electrons acting as charge carriers—have attracted a lot of interest. Tin dioxide (SnO_2), zinc oxide (ZnO), and titanium dioxide (TiO_2) are typical examples. However, p-type metal oxide nanoparticles have an abundance of holes acting as charge carriers, including copper oxide (CuO), nickel oxide (NiO), and cobalt oxide (Co_3O_4) (39).

These nanoparticles' special qualities—such as their high surface-to-volume ratio, programmable electronic structure, and quantum confinement effects—have made them widely used in a variety of industries. N-type and p-type metal oxide nanoparticles are essential for the advancement of technology in a variety of applications, including gas sensing, photocatalysis, solar cells, and transparent conducting electrodes (40).

There are two ways to create metal nanoparticles: the first is a physical process that uses various techniques including laser ablation and evaporation/condensation. The second method is chemical in nature, whereby the solution's metal ions are lowered in a way that promotes the

eventual development of tiny metal aggregates or clusters. Recently, there has been a growing appreciation for the utilization of nanoscale semiconductors in photocatalytic oxidation of harmful contaminants (4). Compared to their bulk counterparts, metal oxide nanoparticles have unusual physical and chemical characteristics that make them an intriguing class of materials. These characteristics result from their nanoscale size, which is usually between 1 and 100 nm. This causes quantum confinement effects and a high surface-to-volume ratio (5). Metal oxide nanoparticles' precise synthesis, size, and shape control has made them useful in a variety of sectors, such as energy conversion and storage, biomedicine, environmental remediation, and catalysis.

Over the past several decades, the field of study on metal oxide nanoparticles has grown exponentially due to breakthroughs in synthesis and characterization techniques as well as the discovery of new features and applications. The goal of this review paper is to present a thorough overview of the status of research on metal oxide nanoparticles, including topics related to production, characterisation, and applications. As highlighted by Niederberger (6), "The field of metal oxide nanoparticles is vast and diverse, encompassing a wide range of materials with unique properties and potential applications." Numerous metal oxide systems, including more complicated ternary and quaternary oxides as well as simple binary oxides like TiO2, ZnO, and Fe3O4, have been explored. These systems demonstrate this diversity.

1.2 METAL DOPED MONPs

Recent years have seen tremendous progress in the field of materials science, especially in the creation and use of new nanomaterials and functional oxides. The general characteristics of beta lead oxide (β-PbO) and metal-doped metal oxide nanoparticles are the two main topics of this review. These materials have attracted a lot of interest because of their special qualities and possible uses in a wide range of technical fields.

One method that has shown promise for improving MONPs' catalytic activity, selectivity, and stability is the insertion of metal dopants into their crystal structure (41). The goal of this review is to present a thorough summary of the state of the art in metal-doped MONP research, with an emphasis on their synthesis, characterisation, and catalytic uses.

Metal-doped metal oxide nanoparticles are a type of advanced materials in which new or improved characteristics are produced by introducing metal dopants into the crystal lattice of metal oxide nanoparticles. To customize the electrical, optical, magnetic, and catalytic

characteristics of metal oxide nanoparticles for particular uses, this doping technique has been thoroughly investigated (7).

1.3 APPLICATION OF MONPs

Compared to conventional catalysts, metal-doped metal oxide nanoparticles (MONPs) exhibit increased activity, selectivity, and stability, making them attractive catalysts for a range of industrial applications (42).

Metal-doped metal oxide nanoparticles exhibit a wide range of enhanced or novel properties compared to their undoped counterparts. Some of the key properties and applications include: (a) Enhanced Photocatalytic Activity: Doping with transition metals or rare earth elements can extend the light absorption range and improve charge separation in photocatalytic materials. For example, Zn-doped TiO_2 nanoparticles have shown improved photocatalytic degradation of organic pollutants under visible light irradiation (8). (b) Improved Gas Sensing: Doping can modify the electronic structure and surface properties of metal oxide nanoparticles, leading to enhanced gas sensing performance. Cu-doped SnO_2 nanoparticles have demonstrated increased sensitivity and selectivity towards H2S gas (9). (c) Magnetic Properties: Doping with magnetic elements can induce ferromagnetism in otherwise non-magnetic metal oxides. Co-doped ZnO nanoparticles have been extensively studied for their room-temperature ferromagnetism and potential applications in spintronics (10). (d) Enhanced Catalytic Activity: Metal doping can create active sites and modify the redox properties of metal oxide nanoparticles, leading to improved catalytic performance. Pd-doped CeO_2 nanoparticles have shown excellent catalytic activity for CO oxidation and methane combustion (11). (e) Optoelectronic Applications: Doping can modify the band structure and optical properties of metal oxide nanoparticles, making them suitable for various optoelectronic applications. In-doped ZnO nanoparticles have been used as transparent conducting oxides in solar cells and display devices (12).

1.4 GENERAL PROPERTIES OF β-LEAD OXIDE

The alpha (α) and beta (β) phases of PbO have emerged as promising materials for various energy storage and conversion technologies, offering distinct characteristics that can be leveraged for specific applications (43).

Beta Phase (β-PbO): The β-PbO, adopts an orthorhombic structure with space group Pbcm. Zhang et al. (2022) conducted a detailed structural analysis of β-PbO using synchrotron-based X-

ray absorption spectroscopy. The authors observed that "the β-PbO structure features zigzag chains of Pb-O bonds, resulting in a more open and flexible framework compared to α-PbO" (44).

Beta lead oxide (β-PbO), also known as massicot, is one of the polymorphic forms of lead (II) oxide. It possesses unique structural, electronic, and physicochemical properties that make it interesting for various applications. The general properties of β-PbO are as follows:

Crystal Structure: β-PbO crystallizes in an orthorhombic structure with space group Pbcm. The structure consists of zigzag chains of PbO4 square pyramids sharing edges, resulting in a layered arrangement (13). This unique structure contributes to the anisotropic properties of β-PbO and its tendency to form plate-like crystals. Electronic Properties**:** β-PbO is a semiconductor with a direct band gap of approximately 2.7-2.8 eV (14). The electronic structure of β-PbO is characterized by the presence of stereochemically active lone pairs on the Pb2+ ions, which play a crucial role in determining its properties. The conduction band is primarily composed of Pb 6p orbitals, while the valence band consists of O 2p and Pb 6s orbitals (15). Optical Properties: The optical properties of β-PbO are influenced by its electronic structure and crystal symmetry. It exhibits strong absorption in the ultraviolet and visible regions of the electromagnetic spectrum, with a characteristic yellow color. The optical anisotropy of β-PbO results in birefringence, making it potentially useful for optical applications. Thermal Properties**:** β-PbO undergoes a phase transition to the tetragonal α-PbO (litharge) structure at temperatures above 489 ^{0}C (16). This phase transition is reversible and has implications for the use of β-PbO in high-temperature applications. The thermal expansion of β-PbO is anisotropic, with different expansion coefficients along the crystallographic axes (17). Chemical Reactivity**:** β-PbO exhibits amphoteric behavior, reacting with both acids and bases. In acidic conditions, it forms lead (II) salts, while in basic conditions, it forms plumbites. The surface of β-PbO is reactive towards atmospheric CO2 and water vapor, leading to the formation of lead carbonates and hydroxides.

1.5 Statement of the problem

This research seeks to examine how doping β-lead oxide (β-PbO) with nickel (Ni) and lithium (Li) alters its structural and optical characteristics. Using the co-precipitation technique, pure β-PbO will be synthesized and subsequently doped with varying concentrations of Ni and Li. The study will focus on analyzing changes in crystal lattice parameters, phase formation, and optical

properties such as band gap energy and light absorption. By understanding these effects, the research aims to provide valuable insights for optimizing β-PbO-based materials for advanced technological applications, including sensors and optoelectronic devices.

1.6 Objective of the Research

1.6.1 General objective

The study's main goal is to find out how doping with Ni and Li affects the optical and structural characteristics of pure beta lead oxide (β-PbO) nanoparticles that were prepared by using co-precipitation method.

1.6.2 Specific objective

The specific objectives of this thesis include the following

- To synthesis Ni and Li dopped (β-Pbo) nanoparticles by using co-precipitation method.
- To study the effects of dopped metals on structural, optical and photoluminses properties

1.7 Significance of the problems

The discovery is significant because it advances our knowledge of how doping with Ni and Li affects the optical and structural characteristics of pure beta lead oxide (β-Pbo) nanoparticles made by co-precipitation methods (cpt). The study is important because it has the potential to improve scientific understanding, spur technical advancements, solve environmental issues, and direct real-world applications across a range of businesses.

1.8 The research gap

Numerous researchers have previously produced developed co-precipitation techniques for the synthesis and characterization of nanoparticles. The researchers synthesized a variety of metal oxides, including binary and ternary metal oxides, but no one else performed research on nikel and lithium doped pure beta lead oxide, and no literature review was conducted regarding the effects of these compounds' structural and optical properties. The structural and visual effects of lithium and nikel on pure beta lead oxides produced by co-precipitation process were the thesis's weak points.

1.9 Scope of the thesis

Thus, addressing the deficiency in current research to examine the effects of Ni and Li doping on the optical and structural characteristics of pure beta lead oxide (β-PbO) Nanoparticles that are very intriguing for the advancement of optoelectronic devices and uses. Moreover, optical

and electrical qualities may improve for a range of applications. The researcher used several characterisation techniques in these studies.

UNIT TWO

2. LITERATURE REVIEWS

The β-PbO has low electrical conductivity relative to α-PbO which hinders its application in optoelectronics and other technological devices. The structural, electrical, and optical properties of $Co^{2+,}$ Ni2^{+}, Cu2^{+}, Li^{+}, and Sn^{2+} doped β-PbO at the Pb site were investigated in this work using Quantum espresso as a DFT tool. The GGA and LDA exchange functionals were used for band structure calculations. The indirect band gap property is indicated by the calculation of electronic band structure, with spin up state band gap values of 2.28 eV, 0.68 eV, 1.01 eV, 1.57 eV, 1.79 eV, and 1.76 eV for pristine, Co^{2+}, Ni^{2+}, Cu^{2}+, Li^{+}, and Sn^{2+}-doped β-PbO, respectively. The spin down states band gap of Co^{2+} and Ni^{2+} was 0.1 eV and 0.32 eV, whereas other dopants and pristine β-PbO equal with spin up states. The PDOS calculation shows how each orbital contributes to the formation of deep level valence band, shallow level valence band, and conduction band states. Dopant effects on optical properties such as JDOS, dielectric functions, refractive index, extinction coefficient, reflectivity, absorption coefficient, electron energy loss spectrum, and optical conductivity were thoroughly discussed. This research provides in-depth functional characteristics for guiding laboratory working experiments and the applications of these materials in various fields such as energy storage and solar cells (18).

Pure, Copper and Zinc doped Cadmium oxide was incorporated by the co-precipitation method. In this preparation method cadmium chloride, copper chloride, zinc chloride has been utilized as a precursor material. X-Ray Diffraction pattern, Fourier Transform Infrared spectrum and, Energy-Dispersive X-Ray Spectrum has affirmed the presence of the copper and zinc doped cadmium oxide nanoparticles. Scanning Electron Microscope uncovered the surface morphology, Ultra Violet-Vis Near Infra analysis and the optical band gap of the materials were observed to be 2.48 eV for Pure CdO, 2.35 eV for Cu CdO and 2.28 eV for Zn CdO which were assessed from Tauc's plot. The predominant electrochemical capacitive execution using Cyclic Voltammetry which indicates that the material has the ability to form a capable electrode material for stable and high-performance electrochemical supercapacitors (19).

The pristine WO_3 (tungsten trioxide) and Cu/Ni Co-doped WO_3 nanoparticles were synthesized by the co-precipitation synthesis methods with fixed wt.% of nickel, i.e., 5 wt.%, and different wt.% of copper, i.e., 2, 3, 5 wt.%. The structural, optical and electrical properties, as well as the

surface morphology were investigated thoroughly by various characterization techniques. All the doped/co1doped and un-doped samples had an orthorhombic structure, according to the XRD measurements. The XRD results further confirmed that the average crystalline size ranged from 46 to 25 nm after the dopant concentration was introduced. Reflectance spectroscopy was used to investigate the optical properties of the prepared nanomaterials and revealed that the optical band gap varied from 2.80 to 2.63 eV with dopant concentrations. The room temperature photoluminescence study showed that the emission peaks were observed in the visible region with slight peak shift towards short wavelength with dopant concentrations. The FTIR studies described the different mode of band related to a functional groups present in the materials and the stretching mode of O–W–W observed from 550 to 1050 cm−1. The I-V studies confirmed that the prepared samples had a good ohmic contact behavior and the resistivity decreased from 6.3×10^{-3} Ω.cm to 0.63×10^{-3} Ω.cm with doping concentration (20).

Manganese ferrite nanoparticles ($MnFe_2O_4$) were synthesized by three different methods including the co-precipitation, sol-gel, and hydrothermal route. Structure, size, morphology, and magnetic properties of nanostructures were determined and compared using X-ray diffraction, Fourier-transform infrared spectroscopy, field emission scanning electron microscopy analysis (FESEM), and the vibration sample magnetometer (VSM). X-ray diffraction analysis from Debye–Scherrer's formula with the ($2\theta = 35.08^0$) peak indicated that the mean size of the synthesized manganese ferrite nanocrystallites were obtained to be 36, 45, and 16 nm for co-precipitation, sol-gel, and hydrothermal, respectively. Also, the sample prepared by the hydrothermal method has the lowest crystal sizes, which it is approved by FESEM analysis. Field emission scanning electron microscopy analysis images confirmed the existence of three types of basic morphology of $MnFe_2O_4$ nanoparticles: spherical shape, multi-walled hollow nanosheets, and reticular structure. In addition, based on VSM data magnetization saturation (M_s) was 41.89 emu/g for hydrothermal synthesized samples, 38.76 emu/g for co-precipitation samples, and 9.52 emu/g for sol-gel samples. These findings show that various methods of nanoparticle synthesis can lead to different particle sizes and magnetic properties (21).

Modified auto combustion method was used to synthesize pure and 1% Co doped Cr_2O_3 X-ray powder difraction (XRD) with an aim to investigate the influence of doping concentration on the behavior of pure and doped Cr_2O_3 nanoparticles. The average crystallite size was estimated with Debye Scherrer's formula. UV–Visible spectroscopy was used to determine the energy band gap

of samples through optical absorption spectrum. From Tauc's plot the value of optical band energy gap (Eg) of the doped and undoped samples is found (22).

Synthesis, structural and optical characterization of pristine and cobalt doped MgO nanoparticles. Nanostructures of pure and Co doped MgO have been synthesized using a modified auto-combustion method. The good crystallinity as well as crystalline size of 21.04nm and 23.56nm for pure and doped samples respectively has been manifested from XRD analysis. An enhancement of the crystalline quality of the nanoparticles and hence a decrease in grain boundary scattering is indicated by an increase in crystalline size with the increase in Co concentration. A general trend of absorption and a decrease in absorbance with increase in the wavelength of incident radiation have been brought out from UV-Visible spectra. Optical bandgaps of 2.75eV and 2.47eV respectively for MgO nanoparticles and Co doped MgO nanoparticles have been revealed from Tauc plot analysis (23).

Nano crystalline powder of Co-Ni ferrites compounds having the chemical formula $Ni_{1-x}Co_xFe_2O_4$ with $x = 0.0, 0.25, 0.5, 0.75$ and 1.0 were prepared by co-precipitation method. The nanoparticles were characterized by X-ray diffraction (XRD), Fourier transform infrared spectroscopy (FTIR) and Scanning Electron Microscopic (SEM) techniques. XRD studies confirmed the formation of single phase spinel structure with space group of $Fd3^-mFd3^-m$. Debye-Scherrer method was applied to determine average crystallite size and the value was found to be in the range of 23-66 nm. Elemental composition characterizations of the prepared samples were performed by Energy Dispersive Spectroscopy (EDS) which shows the presence of Ni, Co, Fe and O. The optical band gap (E_g) of Ni–Co ferrite samples was determined by means of UV-visible spectra. The optical band gap of the prepared samples has been calculated using Tauc plots and has been found to decrease with increase in Co^{2+} content from 3.66 to 3.58 eV (24).

The effect of Ni doping on the, structural, optical, morphology behaviour, by cadmium sulfide (CdS) nanoparticles. The different percentages (0.5, 1.0, 1.5 and 2.0%) of Ni doping CdS nanoparticles are successfully synthesized with average crystalline size from 8.70 to 9.93 nm by sol gel method. The SEM image were combination of metal oxide cubes and rod-like structures with 12-35 nm unequal grain size results in excellent crystalline quality. Optical properties of the sample revealed that the band gap energy decreased from 2.36 to 2.29 eV with an increase in Ni doped percentage. Furthermore, photocatalytic degradation of MB and MO dyes under sunlight

irradiation using Ni doping CdS nanoparticles was performed. The prepared nanoparticle shows 94% degradation activity for MO dye for 75 min. Now a day, sol gel method has attracted a great attention for the production of nanocparticles due of its simplicity and cost effective nature (25).

The pure SnO_2 and Ag-doped snO_2 nanoparticles (NPs) were prepared by co-precipitation method. The structural, electrical and optical properties of the material were systematically studied. The XRD patterns of both samples reveal that the presence of cassiterite tetragonal structure and GSAS fittings confirms the incorporation of Ag in SnO_2 lattices. The SEM-EDS analysis reveals that the presence of spherical-shaped NPs with the expected elements. The Raman spectra of Ag-doped SnO_2 NPs show that the two extra local disorder vibrational modes while comparing with pure SnO_2. The UV-Vis spectroscopy result shows that the Ag doping reduces the optical band gap and increases Urbach tail energy with a reduced effective energy band gap in Ag-doped SnO_2 NPs. The Photoluminescence spectrum confirms the presence of the defects like oxygen vacancies; however, these defects are increased by the Ag-doped SnO_2 system. From the dielectric measurements, the conductivity of both samples followed Jonscher's power law. The nonlinear least-square fittings on Nyquist plots of both samples suggested that the conduction process took place predominantly through grain boundary in SnO_2 NPs whereas through grains in Ag-SnO_2 NPs. This nature of band gap narrowing with increased conductivity in Ag-doped samples drives these samples for good solar cell activity applications. As expected, photovoltaic measurements show higher power conversion efficiency in Ag-doped SnO_2 NPs. These results were discussed by correlating optical and dielectric properties of SnO_2 and Ag-doped SnO_2 NPs which gave a broad understanding for device fabrications successfully (27).

UNIT THREE

3.1 METHODOLOGIES

3.1.1 NANOPARTICLES DEPOSITION TECHNIQUES

3.1.2 CO-PRECIPITATION TECHNIQUES (CPT)

Co-precipitation techniques have emerged as powerful and versatile methods for the synthesis of nanomaterials, offering a range of advantages including simplicity, cost-effectiveness, and scalability. These techniques involve the simultaneous precipitation of two or more components from a solution, resulting in the formation of nanoparticles with controlled composition, size, and morphology (30). The ability to synthesize nanoparticles with tailored properties has revolutionized numerous fields, including catalysis, energy storage, biomedicine, and environmental remediation. Understanding the nucleation and growth mechanisms is crucial for controlling nanoparticle characteristics in CPT (46)

The importance of co-precipitation techniques stems from their ability to produce a wide variety of nanomaterials, including metal oxides, mixed metal oxides, and composite nanoparticles, under relatively mild conditions. These methods often allow for precise control over particle size, shape, and composition through careful manipulation of reaction parameters such as pH, temperature, concentration, and the presence of additives or surfactants (31). Co-precipitation techniques are based on the fundamental principles of nucleation and growth in supersaturated solutions.

3.1.3 Factors affecting CPT

Co-precipitation techniques have gained significant attention in the field of nanomaterial synthesis due to their versatility, simplicity, and cost-effectiveness. These methods involve the simultaneous precipitation of two or more components from a solution, resulting in the formation of nanoparticles with controlled composition, size, and morphology (32). The ability to fine-tune the properties of synthesized nanoparticles makes co-precipitation an attractive approach for various applications, including catalysis, energy storage, biomedicine, and environmental remediation. Understanding the factors that influence co-precipitation processes is crucial for achieving precise control over nanoparticle characteristics. These factors can be broadly categorized into reaction conditions, precursor properties, and external influences. By

manipulating these parameters, researchers can tailor the size, shape, composition, and surface properties of the resulting nanomaterials to meet specific requirements for different applications.

pH Influence: The pH of the reaction medium plays a crucial role in co-precipitation processes, affecting both the solubility of precursors and the surface charge of forming nanoparticles.

Temperature Effects: Reaction temperature significantly influences the kinetics of nucleation and growth processes in co-precipitation.

Concentration Impact: The concentration of precursors and precipitating agents plays a critical role in determining the supersaturation level, which in turn affects nucleation and growth processes.

Surfactants and Capping Agents: The presence of surfactants or capping agents during co-precipitation can significantly influence the size, shape, and stability of the synthesized nanoparticles. Surfactants can adsorb onto the surface of growing nanoparticles, preventing agglomeration and controlling growth rates in specific crystallographic directions.

Stirring Rate: The stirring rate during co-precipitation can affect the homogeneity of the reaction mixture and the mass transfer rates, influencing particle nucleation and growth. However, excessively high stirring rates can sometimes lead to particle fragmentation or promote agglomeration due to increased particle collisions. Finding the optimal stirring rate for a specific system is often crucial for achieving the desired particle characteristics.

Aging Time: The aging time, or the duration for which the precipitated particles are left in the reaction medium, can significantly affect the final properties of the nanoparticles. During the aging process, smaller particles may dissolve and redeposit onto larger particles through Ostwald ripening, leading to changes in particle size distribution and crystallinity.

3.1.4 NANOPARTICLS CHARACTERIZAION

A helpful quantitative description of the material's composition is characterization. In essence, characterisation is the description of the types and locations of the components, atoms, and ions, to the degree that this description is required for the material's performance, connection with attributes, and ability to be reproduced and improved. The characterizing instruments employed in this research are

3.1.4.1 X-ray Diffraction (XRD):

X-Ray Diffraction (XRD) is the most commonly used technique in the determination of crystal structure of atoms.X-ray diffractometer consist of three basic elements

i. An X-ray tube
ii. An X-ray detector
iii. A sample hold

X-rays are generated in a cathode ray tube by heating a filament to produce electrons, accelerating the electrons toward a target by applying a voltage, and bombarding the target material with electrons. When electrons have sufficient energy to dislodge inner shell electrons of the target material, characteristic X-ray spectra are produced. These spectra consist of several components, the most common being Kα and Kβ. Kα consists, in part, of Kα1 and Kα2. Kα1 has a slightly shorter wavelength and twice the intensity as Kα2. The specific wavelengths are characteristic of the target material (Cu, Fe, Mo, and Cr). Filtering by foils or crystal monochrometer is required to produce monochromatic X-rays needed for diffraction. Kα1 and Kα2 are sufficiently close in wavelength such that a weighted average of the two is used. Copper is the most common target material for single crystal diffraction, with CuKα radiation = 1.5418 Å. These X-rays are collimated and directed onto the sample. As the sample and detector are rotated, the intensity of the reflected X-rays is recorded. When the geometry of the incident X-rays impinging the sample satisfies the Bragg Equation, constructive interference occurs and a peak in intensity occurs. A detector records and processes this X-ray signal and converts the signal to a count rate which is then output to a device such as a printer or computer monitor (33).

Figure 3.1: XRD Machine

The most commonly used X-ray instrument is the powder diffractometer. It has a scintillation or Geiger counter. The detector shows a range of scattering angles. Generally, it is a practice to mention scattering angle 2θ. The intensities are taken as peak heights. The d values can be calculated from the graph. A set of peaks and their heights is adequate for phase identification.

In Bragg's law a crystal is viewed as a plane containing lattice points. The reflection of X-rays will take place from these planes with the angle of reflection is equal to angle of reflection as shown in the figure 2.5 below. From the figure BCD= BC+CD= d sinθ +d sinθ = 2d sinθ. The reflected beams are in phase when the path length between them is an integral multiple of the wavelength. This means the distance BCD = n λ. That is

$$n \lambda = 2d \sin\theta.$$

Where n = 0, 1, 2, 3…, d = interplanar spacing, λ = wavelength of incident X-rays, ɵ = angle of reflection. This is the Bragg's law

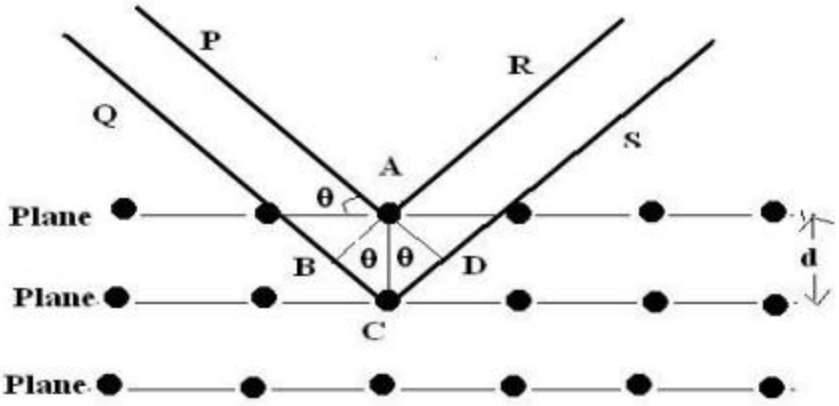

Figure: 3.2 Bragg's law analysis.

For crystal contain thousands of planes the Bragg's law imposes certain restrictions on angle of reflection. In that case diffraction peak will be broaden and the s effect is used to measure the size of particle by using Debye- Scherer formula The average crystallite size is calculated from XRD pattern using Debye – Scherer formula,

$$D = \frac{\kappa\lambda}{\beta cos\theta}$$

Where λ is the wavelength of X -rays used (1.5406Å), k is the shape factor (0.89), β is the Full Width Half Maximum (FWHM) in radian and θ is the angle of diffraction.

In the powder sample, there are a large number of crystallites (≈1012per mm^3) oriented in all possible directions. When a monochromatic X-ray beam falls on the powder sample, all possible combinations of θ and d are obtained, which satisfy Bragg's condition, and for any particular d, all orientations of the crystallites are obtained and, hence, the diffracted rays lie on the surface of a cone with the semi-vertical angle of 2θ, as shown in figure. If the sample has big grains, the diffraction ring or the arc will be spotty. To avoid it or make the arcs smooth, arrangement is made for the rotation of the sample on its axis.

The determination of lattice parameters in orthombic systems requires careful consideration of the relationship between interplanar spacings and Miller indices. As described by Pecharsky and Zavalij (2009), "For an orthombic crystal, the relationship between d-spacing and lattice parameters is given by:

$$\frac{1}{d^2} = \frac{h^2}{a^2} + \frac{k^2}{b^2} + \frac{l^2}{c^2}$$

Orthorhombic structures represent one of the seven fundamental crystal systems in crystallography, characterized by three mutually perpendicular axes of unequal lengths ($a \neq b \neq c$) and all angles equal to 90° ($\alpha = \beta = \gamma = 90°$). This unique geometric configuration gives rise to a wide range of interesting properties and applications across various scientific disciplines. The study of orthorhombic volumes and their structural implications is crucial for understanding the behavior of materials at the atomic and molecular levels, as well as for developing novel materials with tailored properties.

3.1.4.2 Ultraviolet-Visible Spectroscopy (UV-Vis)

Ultraviolet-visible spectroscopy is the widely used technique to characterize organic and inorganic nanoparticles. UV-VISIBLE absorption spectroscopy used electromagnetic radiation between 200-800 nm. This radiation is divided between Ultraviolet (200-400nm) and Visible (400- 800 nm). This spectroscopy is also known as Electronic spectroscopy due to the absorption of UV radiation or Visible radiation by molecules lead to the transition between electronic energy levels of the molecules. The UV spectroscopy obeys Beer-Lambert law (34). The Beer Lambert law states that when a beam of monochromatic radiation is passed through solution of an absorbing substance the rate of decrease in intensity of radiation with the thickness of absorbing solution is proportional to the incident radiation as well as the concentration of the solution

$$A = \log (I0/I) = ECL$$

Where, A = Absorbance, I0 = Intensity of light incident upon sample cell, I = Intensity of light leaving sample cell, C = molar concentration of solution, L = length of sample cell, E = molar absorptivity.

Reflectance and absorbance spectroscopy have emerged as powerful and versatile techniques for characterizing nanomaterials, offering insights into their optical, electronic, and structural properties. As noted by Christensen (1997), "Disruptive technologies often enable the emergence of new markets and value networks." In this context, these spectroscopic methods have become indispensable tools in the field of nanomaterial research, providing rapid, non-destructive, and highly sensitive analysis (47). Diffuse reflectance spectroscopy is particularly useful for characterizing powdered or rough-surfaced nanomaterials.

. Reflectance spectroscopy measures the fraction of incident light that is reflected from a material's surface. Wang et al. (2021) investigated the use of diffuse reflectance spectroscopy in characterizing TiO2 nanoparticles. The researchers noted that "reflectance measurements are particularly sensitive to surface properties and are less influenced by sample thickness, making them ideal for studying powdered or rough-surfaced nanomaterials" (48). Absorbance spectroscopy, on the other hand, measures the amount of light absorbed by a material as it passes through it. Chen et al. (2023) studied gold nanorods using absorbance spectroscopy and reported that "absorbance measurements provide direct information about the electronic transitions and plasmonic properties of nanomaterials in solution or thin films, offering insights into their internal structure and composition" (49). The relationship between absorbance (A) and transmittance (T) is given by the Beer-Lambert law:

$$A = -\log(T).$$

In reflectance spectroscopy, the Kubelka-Munk function F(R) is often used to relate reflectance (R) to absorption coefficient (K) and scattering coefficient (S):

$$F(R) = (1-R)^2 / (2R) = K/S.$$

Reflectance and absorbance spectroscopy can be used complementarily for accurate bandgap determination in semiconductor nanomaterials. Zhang et al. (2023) compared diffuse reflectance and absorbance measurements for bandgap estimation in ZnO nanoparticles. The researchers reported that "while absorbance measurements were more sensitive to small changes in particle size, diffuse reflectance provided more accurate results for highly scattering samples, highlighting the importance of using both techniques for comprehensive characterization" (Zhang et al., 2023, p. 9012).

Figure 3.3: Ultraviolet-Visible Spectroscopy (UV-Vis)

UV-Visible spectra are also used for calculating band gap of semiconductor nanomaterials. In this a monochromatic light is passed through the sample and reference. After transmission they are reflected back in to the detectors where they compare the difference.

3.1.4.3 Photoluminescence Spectroscopy (PL)

PL spectroscopy is a powerful tool for probing the electronic structure and optical properties of semiconductor nanoparticles. It provides information on band gap energies, surface states, and defects. Photoluminescence spectroscopy has emerged as an indispensable technique for probing the optical and electronic properties of materials. Its non-destructive nature and high sensitivity make it particularly valuable in the study of semiconductors, nanostructures, and emerging materials.

The fundamental principle of PL involves the excitation of electrons in a material using light of a specific wavelength, followed by the observation of the subsequent light emission as these electrons return to their ground state. This process provides valuable information about the electronic structure, defects, and impurities in materials (35). Recent years have witnessed significant improvements in PL instrumentation, data analysis techniques, and theoretical understanding, leading to new insights into material properties and behaviors.

3.1.4.4 Scanning Electron Microscopy (SEM)

Scanning Electron Microscopy (SEM) has revolutionized our ability to visualize and analyze materials at the nanoscale. Since its inception in the 1930s, SEM has undergone significant advancements, enabling researchers to probe deeper into the structure and composition of materials with unprecedented clarity and precision. SEM provides high-resolution imaging of nanoparticle morphology, size, and surface features. Modern field-emission SEM instruments can achieve resolutions below 1 nm, making them suitable for imaging a wide range of nanoparticles.SEM is particularly valuable for: Determining nanoparticle size and size distribution, analyzing particle morphology and surface features, investigating nanoparticle aggregation and self-assembly, and Examining the interface between nanoparticles and substrates. However, sample preparation for SEM can be challenging, particularly for organic or biological nanoparticles that may be sensitive to the high-vacuum environment (36).

3.2 Experimental procedure

Instruments and apparatus

The instruments and apparatus used in this study included: UV/Visible spectrophotometer, X-ray diffractometer (XRD), PL, SEM and digital balance, hotplate, centrifuge, thermometer, cylinder, Heater, magnetic stirrer, Glass jars, beakers and drying oven.

Chemicals Required

The high purity chemicals (>>99% purity) such as Lead acetate [Pb $(CH_3COO)_2$], Nickel(Ni), lithium(Li), sodium hydroxide(NaOH), and ethanol(C_2H_6O) were used without any purification. The chemicals used are analytical grade purity.

Synthesis of pure β-Pbo and doped 2% (Li, Ni) β-PbO nanoparticles (NPs)

Pure β-PbO, and 2% (Li: Ni) doped β-PbO nanoparticle were synthesized by simple chemical co-precipitation method. The precursors used in the synthesis were lead (II) acetate trihydrate, sodium hydroxide, lithium, and nickel as starting materials. NaOH is reducing agent. In a typical synthesis appropriate amount of lead acetate trihydrate (9.212g) was dissolved in 50 ml of distilled water. In a closed-necked flask, the solution was vigorously stirred for 1hr with a magnetic stirrer. After 1hr 20ml amount of NaoH was added (drop wise) to the solution then stirred until a homogeneous solution was formed. Then the solution continues stirred and heated for 2 hr at 85 ^{0}C. Afterwards, the solution aged for 24 h and then centrifuged to the obtained

precipitates. The obtained precipitates were washed several times with distilled water and ethanol to remove excess sodium and chlorine ions then dried in an electric oven at 100 ^{0}C for 1hr. Finally, the obtained powder was calcined at 500 °C for 2hr in order to obtain pure β-PbO nanoparticles. To prepare 2% (0.188g) Ni doped PbO samples by lead (II) acetate trihydrate (0.5M) and Nickel Chloride (0.1M) were dissolved in 50 ml distilled water. In a closed-necked flask, the solution was vigorously stirred for 1hr with a magnetic stirrer. After 1hr 9.5 M NaOH was prepared in 20 ml distilled water then added drop wise into the initial aqueous solution constant stirring and heating up to 2hrs at 85°C. After wards the solution aged for 24 h and then centrifuged to the obtained precipitates. The obtained precipitates were washed several times with distilled water and ethanol to remove excess ions and dry in oven at 500 ^{0}C for two hours. The pure β-Pbo and 2 % (Li: Ni) doped β-Pbo nanoparticles have synthesized by chemical co-precipitation method. For Li using the same procedure explained above. The all the obtained samples were used for different characterization.

UNIT FOUR

4. Results and discussions

One of the goals of this work was to demonstrate the different outcomes of co-precipitation investigation approaches for 2 percent (Ni, Li) doped β-Pbo nanoparticles; however, we also included the outcomes for undoped or pure β-Pbo nanoparticles for comparison's purpose. This has made it possible for us to examine the different structural and optical characteristics of β-Pbo nanoparticles that are pure or undoped and doped with 2% (Ni, Li).

4.1 Experimental Results

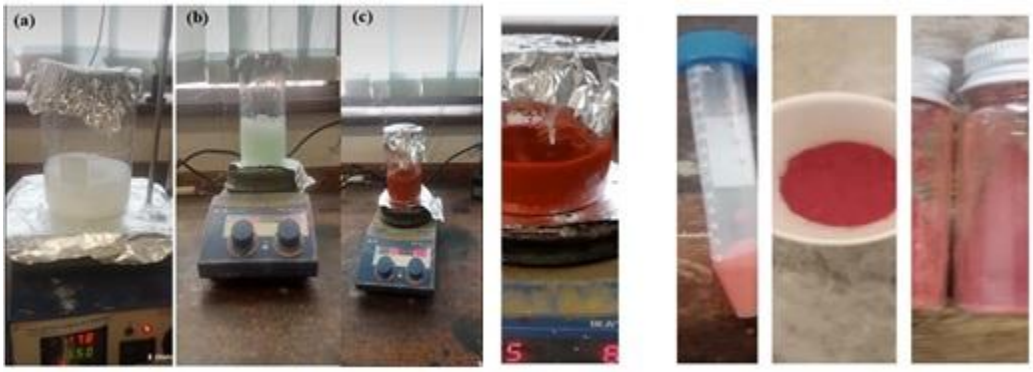

Figure (4.1) represents experimental results of pure, Ni doped and Li doped beta lead oxide nanoparticles powder

4.2 Structural Analysis

We acquired and examined the XRD patterns of pure β-PbO, Ni-doped β-PbO, and Li-doped β-PbO to look into the materials' structural characteristics. The patterns display distinct peaks that align with the orthorhombic structure of β-PbO. Minor modifications are noted when doping with Ni and Li. Figure 4. 2 shows the XRD spectra of pure β-Pbo NPs and doped 2% (Ni, Li) NPs that were made using co-precipitation procedures. The structure, phase, and crystal size of the samples were ascertained by analyzing the peaks' positions and intensities. In the pure, Ni-doped, and Li-doped β-PbO X-ray diffraction patterns. The (100), (111), (200), (020), (002), (220), (300), (202), (022), (311), (131), and (113) planes were represented by the peaks, which correlated to the angles of 2ɬ= 15.03, 29.11, 30.33, 32.62, 37.86, 45.14, 46.22, 49.26, 50.82, 53.14, 56.06, and 63.03 degrees, respectively. The orthorhombic crystal structure of the produced samples, with space group P and lattice parameters a = 5.8931 Å, b = 5.4904 Å, and c

= 4.7528 Å and α = β = γ = 90 0C, was validated by the XRD result. The outcome closely resembles standard batch No. 00-93820.

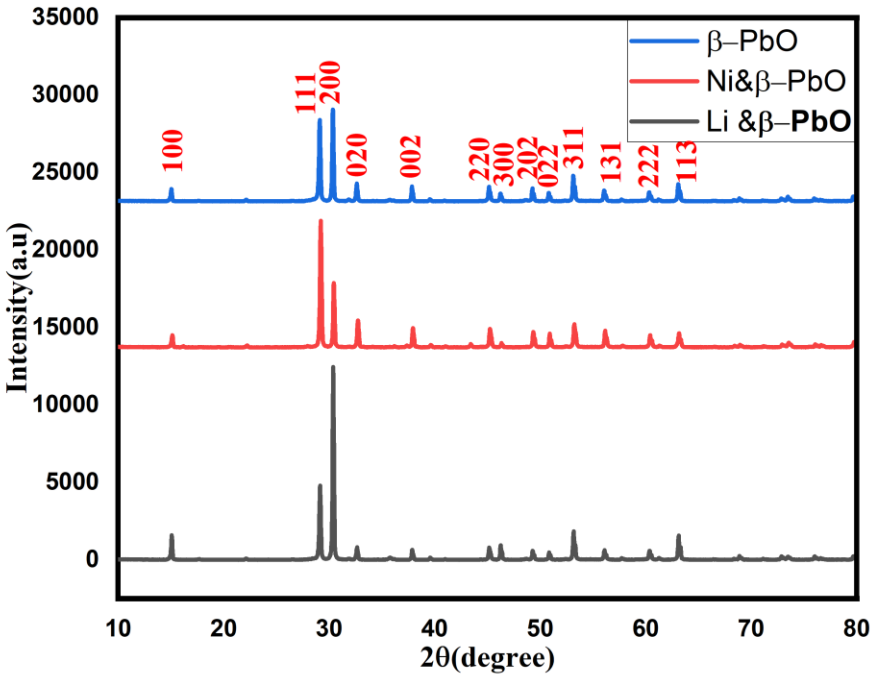

Figure 4.2: XRD patterns of undoped and 2% (Ni, Li) doped β-PbO nanoparticles

X-ray diffraction (XRD) patterns for pure β-PbO, Ni-doped β-PbO, and Li-doped β-PbO nanoparticles appear to be displayed in Figure 4.2. Plotting the three diffraction patterns together, the peaks are identified by their respective Miller indices. Pure β-PbO (Blue Pattern): The XRD peaks show the crystal planes in the β-PbO lattice and are identified with Miller indices such as (100), (020), (111), (200), etc. It is suggested that the material is extremely crystalline by the crisp and well-defined peaks. The lack of further peaks indicates that there are no contaminants or secondary phases present in the β-PbO phase. Ni-Doped β-PbO (Red Pattern): The peak locations in the XRD pattern are shifted when compared to pure β-PbO, most likely because Ni has been incorporated into the β-PbO lattice. To calculate the crystallite size from XRD data, you can use the Scherrer equation. The Scherrer equation relates the crystallite size D to the broadening of a diffraction peak:

$$D = \frac{\kappa\lambda}{\beta cos\theta} \text{ ---------- (1)}$$

Where:

D = crystallite size

K = shape factor (usually 0.9)

λ = X-ray wavelength (1.5406 Å)

β = full width at half maximum (FWHM) of the peak (in radians)

θ = Bragg angle (in radians)

The d-spacing between crystal planes is inversely related to the 2θ angle according to Bragg's law:

$$n\lambda = 2dsin\theta \text{ ---------- (2)}$$

Dislocation density (δ\deltaδ) is a measure of the number of dislocations in a unit area of a crystal and can be calculated using the formula:

$$\boldsymbol{\delta = \frac{1}{D^2}} \text{ ---------- (3)}$$

Where: D is the average crystallite size (in meters)

Strain (ϵ): is commonly used to estimate the microstrain in a material based on the full width at half maximum (FWHM) of the XRD peaks. Strain is calculated using:

$$£ = \frac{\beta}{4tan\theta} \text{ ---------- (4)}$$

The volume V of an orthorhombic crystal structure can be calculated using the formula:

$$V = a \times b \times c \text{ ----------5}$$

Where a, b, and c are the lengths of the three perpendicular axes of the unit cell.

In an orthorhombic crystal system, where a ≠ b ≠c aand α=β=γ=90∘,

Lattice Parameters: For an orthorhombic structure: a, b, and c are calculated from the hkl values using Bragg's law and the d-spacing formula:

$$d_{hkl}=\frac{1}{\sqrt{\frac{h^2}{a^2}+\frac{k^2}{b^2}+\frac{l^2}{c^2}}} \quad \text{---------- (5)}$$

Where h, dk, l are the Miller indices.

Table 4. 1: Structural parameters of pure β- PbOand doped β-PbO

Particles	hkl	2theta(deg)	$d_{hkl}(A^0)$	FWHM(deg)	D(nm)	D(nm) average	$\delta = \frac{1}{D}2$ X 10^{-4}
Pure β-PbO	200	30.3752	2.94030	0.13180	60.33	56.90	3.10
	020	29.1304	3.06305	0.14810	53.70		
	002	53.1510	1.72182	0.14130	56.68		
2%Li; β-PbO	200	30.4089	2.93712	0.12950	61.40	57.78	3.00
	202	29.1614	3.05986	0.14420	55.15		
	002	53.1813	1.72091	0.14000	56.80		
2%Ni; β-PbO	200	29.2298	3.05286	0.15290	51.98	55.40	3.25
	020	30.4664	2.93170	0.13840	57.44		
	002	32.7473	2.73253	0.14620	56.80		

The addition of Li ions, which are smaller than Pb ions, causes the crystallite size to increase to 57.78 nm, indicating that lithium doping causes the crystal lattice to expand. The lattice parameter drops to 55.40 nm with nickel doping, suggesting that the lattice contracts upon the entrance of Ni ions (which are smaller and have a different electrical configuration than Pb ions). The dislocation density is marginally lower in the doped sample than in the pure one. This may suggest that Li doping has a little influence on lowering the crystal structural defects, either by stabilizing the crystal lattice or releasing some internal tension. The dislocation density is higher

in nickel-doped samples than in pure or Li-doped ones. This implies that Ni doping increases the number of defects or dislocations in the crystal structure, presumably as a result of the Ni and Pb atoms' mismatched ionic radii or electronic structures. Li-doped β-PbO exhibits a lower dislocation density, which is indicative of improved crystal quality and reduced flaws. These properties can be advantageous for electrical and optical applications.

Table 4.2 strain, lattice parameters and volume of unit cell doped and undoped beta lead oxide

	Strain £	Lattice parameters(A^0)			Volume of unit cell V = a*b*c $(A^0)^3$
		A	b	C	
Pureβ-PbO	0.107	5.88	6.12	3.44	123.79
Li;β-PbO	0.101	5.87	6.11	3.44	123.37
Ni;β-PbO	0.105	6.10	5.86	5.46	195.17

These differences in lattice parameters and volume due to doping suggest that the dopants (Ni and Li) have different impacts on the β-PbO lattice structure. The substantial volume increase that follows Ni doping suggests that Ni atoms may be causing more lattice expansion due to their larger ionic radius or unique bonding characteristics.

4.3 Optical Analysis

UV-Vis (Ultraviolet-Visible) Spectroscopy Awidely used technique to study the optical properties of materials by measuring the absorbance or reflectance of light in the UV and visible regions. In this process, the spectrum obtained due to optical absorption can be analyzed to get the energy band gap of the material. In optical devices, band gap energy remains one of the main characteristics of the synthesized materials, which must be determined. The reflectance spectra of the un-doped, Ni doped and Li doped samples in the wavelength range of 350 nm to 800 nm are shown in Figure 4.3.

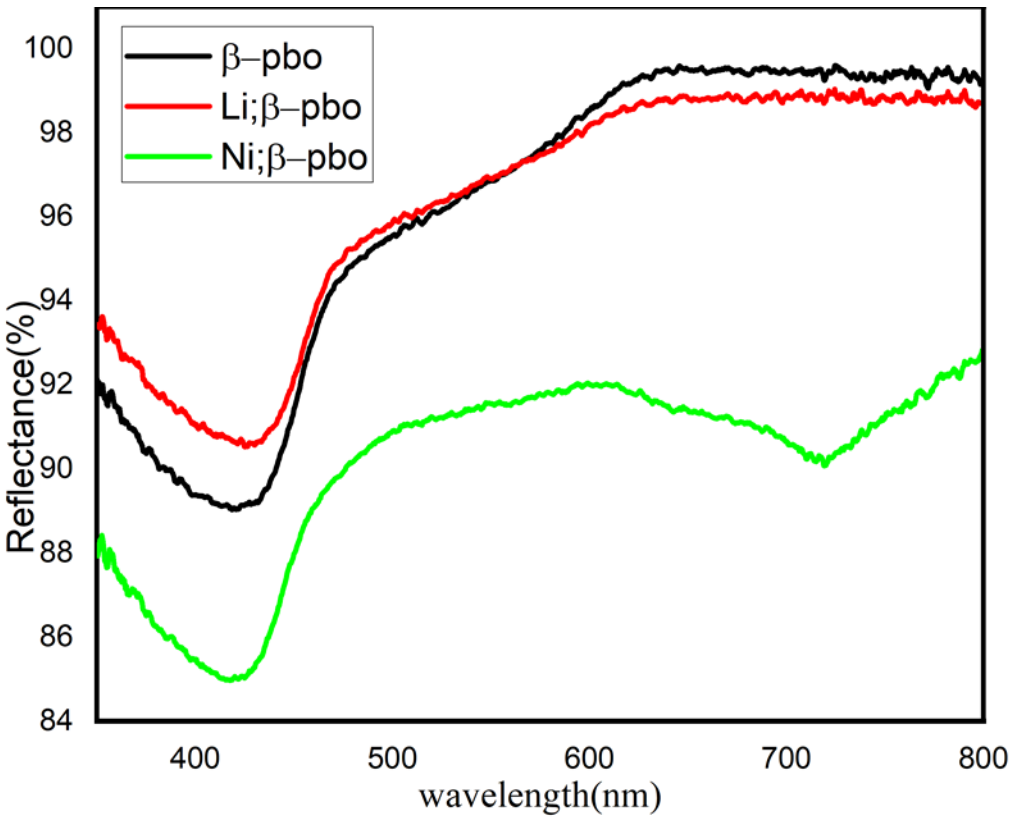

Figure.4.3 Reflectance spectra of pure, Li doped and Ni doped β-PbO.

The β-PbO sample shows a higher overall reflectance than the doped samples, particularly in the visible band.

. While both lines show a similar trend, the reflectance of the Li-doped β-PbO (red line) is somewhat lower than that of the pure β-PbO (black line). With the lowest reflectance across the spectrum, the Ni-doped β-PbO (green line) has a clear declining trend at 500 nm, but then rises again toward the higher wavelengths. In all three samples, there is a discernible decrease in reflectance in the 500-550 nm range; this decrease is more prominent in the Ni-doped β–PbO sample. The variations in reflectance might be ascribed to doping with Li and Ni, which alters the optical characteristics and electrical structure. Ni doping appears to affect the optical characteristics more significantly, either as a result of band structure changes or the introduction of mid-gap states. Ni-doped β-PbO has a much lower reflectance than the other two samples beyond 600 nm. This graph displays a material's reflectance spectrum over a range of wavelengths from around 350 nm to 800 nm, which is most likely beta lead oxide, or β-PbO. The reflectance percentage, which shows how much light the material reflects at each wavelength, is represented by the y-axis. At shorter wavelengths (around 400 nm), the reflectance is minimal. It progressively increases as the wavelength increases, culminating at 800 nm. The materials exhibit a reflectance drop at about 500 nm, which might be related to a bandgap or distinctive absorption property. This type of spectrum is frequently used to examine a material's optical characteristics, such as its bandgap energy or absorption edge.

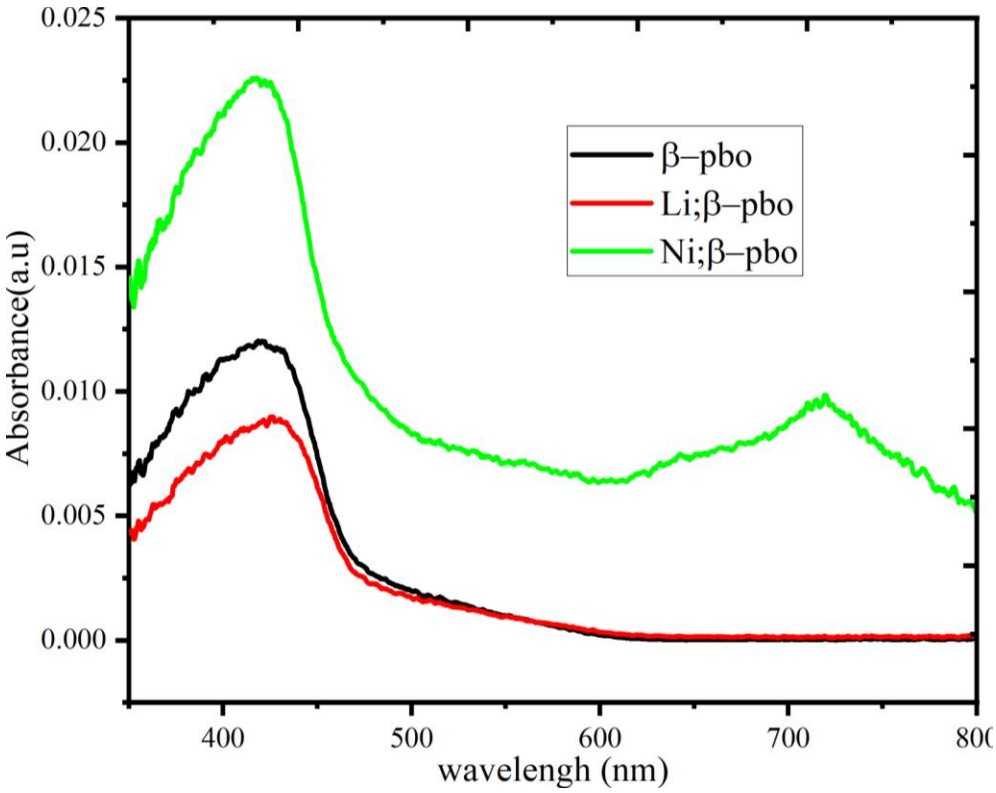

Figure 4.4: Absorption spectra of pure β-PbO and doped β-PbO

β-PbO (Black Line): The absorbance starts to significantly rise at 400 nm, peaks at 470 nm, and then starts to fall. A little hump can be found at 650-700 nm. Li-doped β-PbO (Red Line): Overall absorbance is somewhat lower, but the absorbance curve is comparable to that of pure β-PbO. There is the peak at 470 nm, although it is little lower. Ni-doped β-PbO (Green Line): Absorbance is much greater in this sample, particularly at 470 nm and 600-700 nm. There is a more noticeable hump at 700 nm and a significantly wider absorption peak. 400–500 nm: All three samples exhibit considerable absorption in this range, suggesting that they most likely absorb heavily in the visible spectrum's blue area. Between 500 and 700 nm: Ni-doped β-PbO shows increased absorbance in this range, suggesting that doping with Ni creates states that increase photon absorption in this range. Li Doping: The lower absorbance in comparison to pure β-PbO implies that Li may limit the amount of electronic states that are accessible for transition, whether as a result of fewer defect states or a minor enlargement of the band gap. Ni Doping: The enhanced absorbance, particularly the broad absorption peak, indicates that Ni adds more states to the band gap or levels of defects to the band gap to improve absorption across a longer wavelength range. Structural Effects: Absorbance variations, especially when Ni is doped, indicate atomic-level structural alterations that introduce defect states or modify the band

structure. Optical Effects: Ni-doped β-PbO exhibits a wider and enhanced absorbance, indicating that Ni has a considerable effect on the material's optical characteristics. It is also possible that Ni has introduced new electronic states inside the band gap.

Optical band gap energy is a fundamental property of materials, particularly semiconductors and insulators, that defines the energy difference between the valence band (highest occupied molecular orbital) and the conduction band (lowest unoccupied molecular orbital). It is crucial for determining the electronic and optical behavior of a material. The optical band gap energy of the materials was determined by means of the Tauc's equation, which translates the relation between the absorption coefficient (α) and the incident energy (hν). This relation is given by the equation

$$(\alpha h\nu)^2 = A\,(h\nu - Eg) \text{ and } F(R).\, h\nu = A\,(h\nu - Eg)$$

Where A is constant and has different values for different transitions, hν is the photon energy, F(R) is the Kubelka-Munk function, R is the diffuse refractance, and Eg is the optical band gap energy.

$$F(R) = (1\text{-}R)^2 / 2R$$

The energy bandgap of undoped β-PbO, Ni and Li doped β-Pbo nanoparticles were found to be 2.7, 2.7 and 2.68 eV respectively shown in (Figure 4.5, 4.6, 4.7).

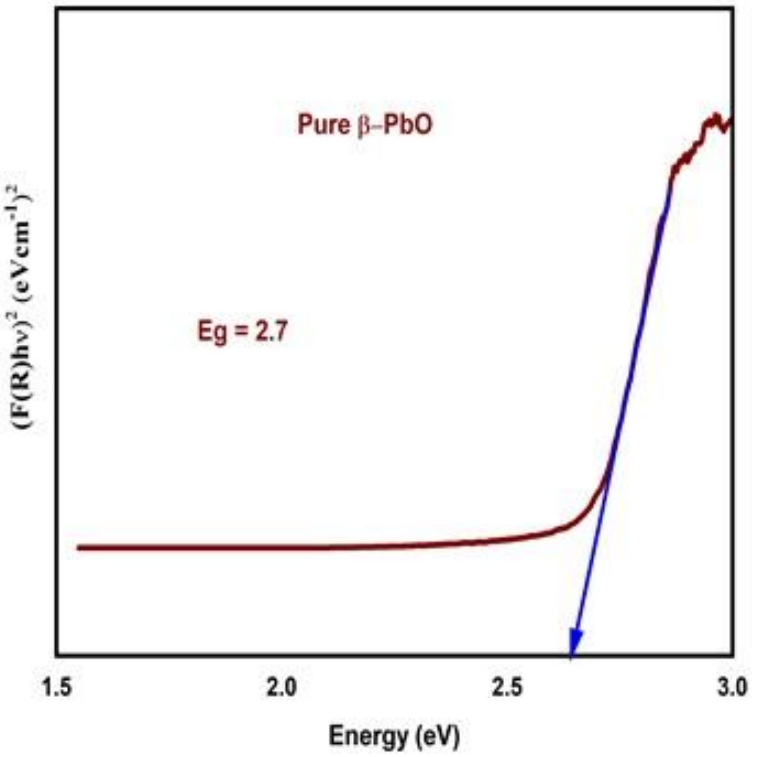

Figure-4.5 Band gap spectra for pure β-PbO

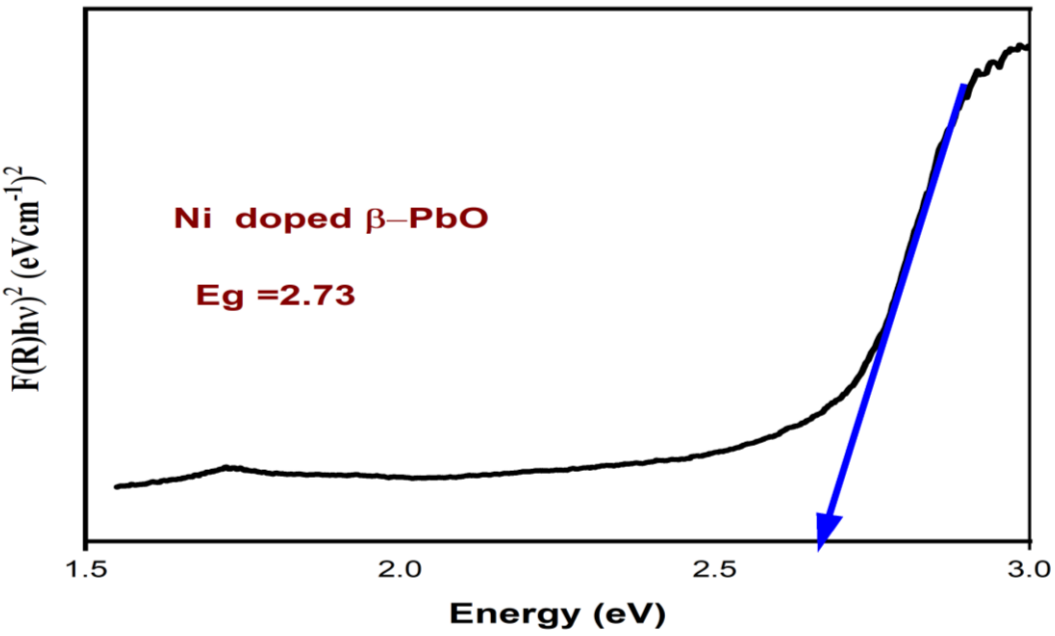

Figure-4.6 Band gap spectra for Ni doped β –PbO Nanoparticles

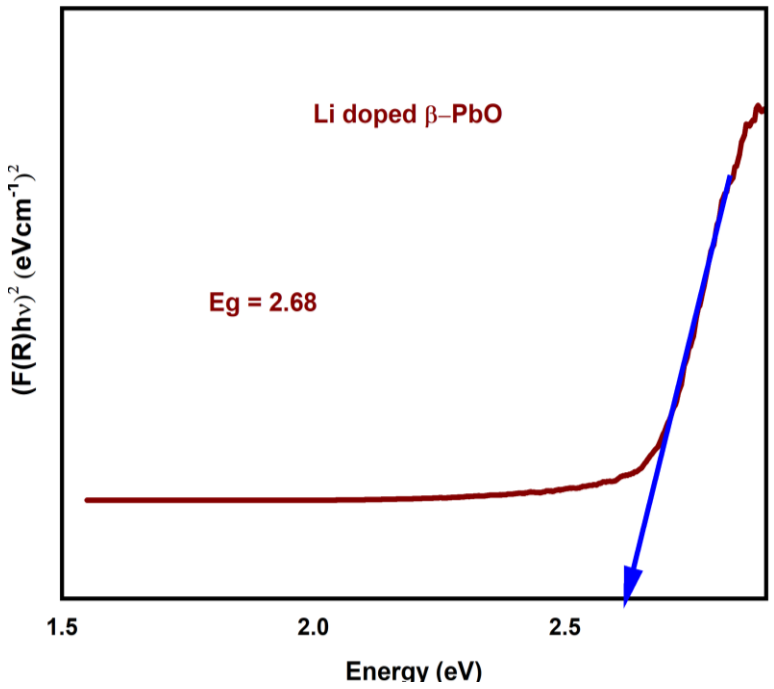

Figure-4.7 Band gap spectra for Li doped β –PbO Nanoparticles

Table 4.3 Bandgap of pure, Ni doped and Li doped beta lead oxide

Sample	Band gap
Pure β-PbO	2.7 ev
Ni: β-PbO	2.73 ev
Li:β-PbO	2.68 ev

When β-PbO is pure, its band gap is around 2.7 eV; when doped with Ni, this value rises to 2.73 eV. These numbers show that doping has somewhat altered the electrical characteristics. The band gap somewhat narrows as a result of Li doping, indicating that the presence of Li in the lattice has caused some electronic rearrangement or state introduction.

4.4 Photoluminescence (PL) studies

Photoluminescence (PL) studies of pure and doped materials like beta lead oxide (β-PbO) provide insight into their electronic structure, defect states, and potential applications in optoelectronics.

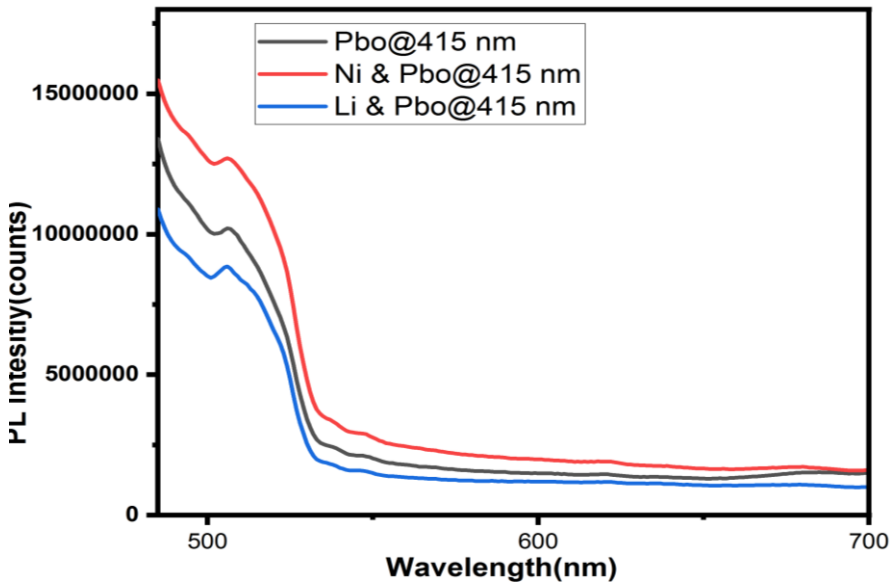

Figure 4.8: PL spectra of pure β-PbO and doped β-PbO at 415 nm

When stimulated at 415 nm, the sample with the highest photoluminescence intensity, Ni-doped β-PbO (Red Line), displays a strong luminous response. Pure β-PbO (Gray Line): The PL intensity is higher than that of Li-doped β-PbO but somewhat less than that of Ni-doped β-PbO. Li-doped β-PbO (Blue Line): This sample exhibits the lowest PL intensity, which suggests that Li doping has reduced the luminous efficiency. The primary emission peak appears close to the wavelength of excitation (415 nm) and rapidly diminishes with increasing wavelength. This steep decline is typical of emission close to the band boundary. As the PL intensity decreases with increasing wavelength, all samples show a similar pattern, despite the significant variations in absolute intensities. Li doping may cause an electronic structure change that reduces radiative recombination efficiency. Ni-doped β-PbO has enhanced photoluminescence due to the introduction of defect states that permit radiative recombination, making it a potential material for high emission optoelectronic applications. Li-doped β-PbO exhibits decreased photoluminescence. indicating that the band structure may be altered by Li doping in a way that reduces radiative effectiveness.In the absence of additional dopants, the pure β-PbO exhibits typical behavior, as indicated by its low PL intensity.These results show that doping significantly changes the optical properties of β-PbO, particularly in terms of its photoluminescence response, which may be tailored to specific requirements by adjusting the kinds and concentrations of doping.

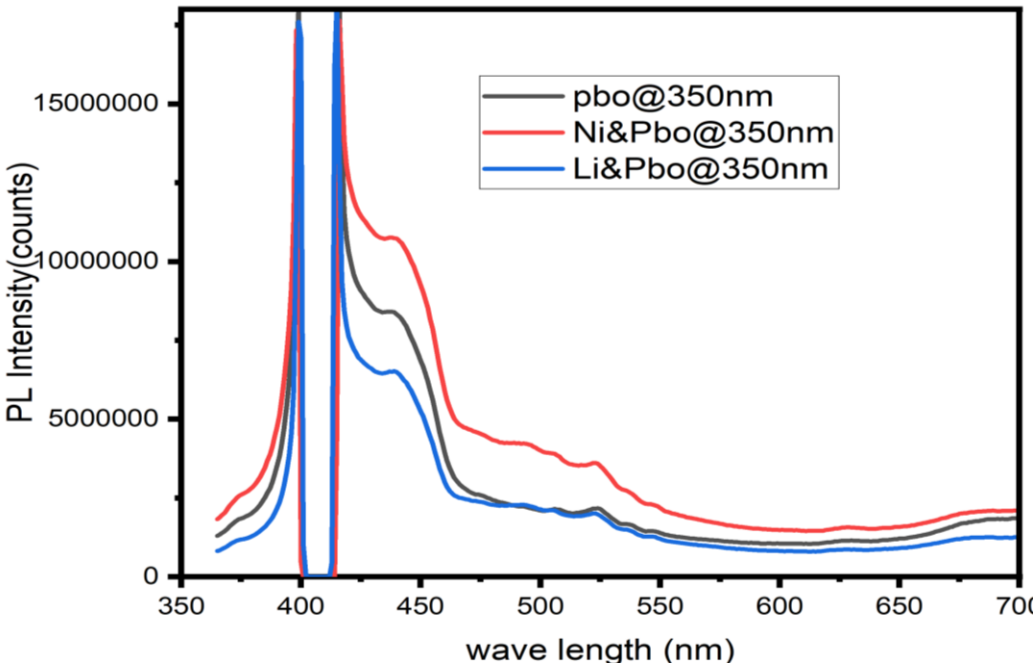

Figure 4.9; PL spectra of pure β-PbO and doped β-PbO at 350 nm

The β-PbO black curve is used as a benchmark for contrasting the doped samples. When compared to pure β-PbO, the red curve (Ni-dopedβ- PbO) shows a discernible increase in PL intensity. Comparable in trend, but somewhat less pronounced than the Ni-doped sample, is the blue curve representing Li-doped β-PbO. In all three graphs, a clear peak is seen at 400 nm, while the doped samples exhibit considerable intensity fluctuation and minor peak position variations. Doping with Ni and Li modifies the electronic structure of β-PbO, hence increasing the number of accessible states for recombination, as suggested by the increased PL intensity in the doped samples. Doping Effects: Examine how the various dopants impact PbO's electrical and optical characteristics. Defect States: Take into account looking into the possibility that doping-induced defect states play a part in the observed variations in PL intensity. Charge Carrier Dynamics: Gaining knowledge of how doping affects the dynamics of charge carriers, particularly recombination processes, may help explain the behavior that has been seen.

4.4. Scanning Electron Microscopy (SEM)

A potent method for analyzing nanoparticles is scanning electron microscopy (SEM), which offers high-resolution imaging capabilities that reveal vital details on the size distribution, surface characteristics, and shape of the particles. SEM investigations are very useful in the

context of β-PbO nanoparticles to comprehend the effects of doping with elements like Ni and Li on the structural characteristics of these materials. Energy-dispersive spectroscopy in conjunction with scanning electron microscopy was used to analyze the elemental composition and surface morphology of pure, Ni, and Li doped β-Pbo samples. The samples' SEM pictures are displayed in the figure below.

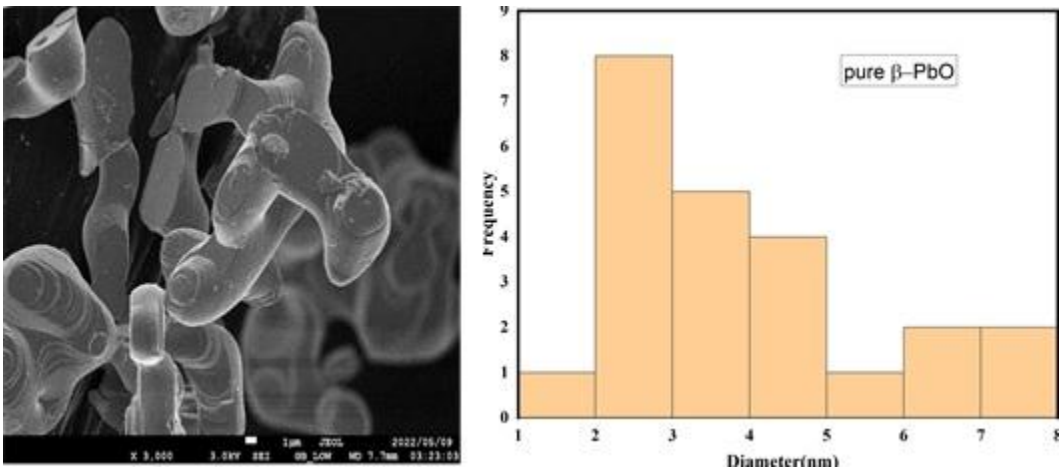

Figure (4.10); SEM images of pure β-PbO NPs and the average grain size of pure β-PbO NPs

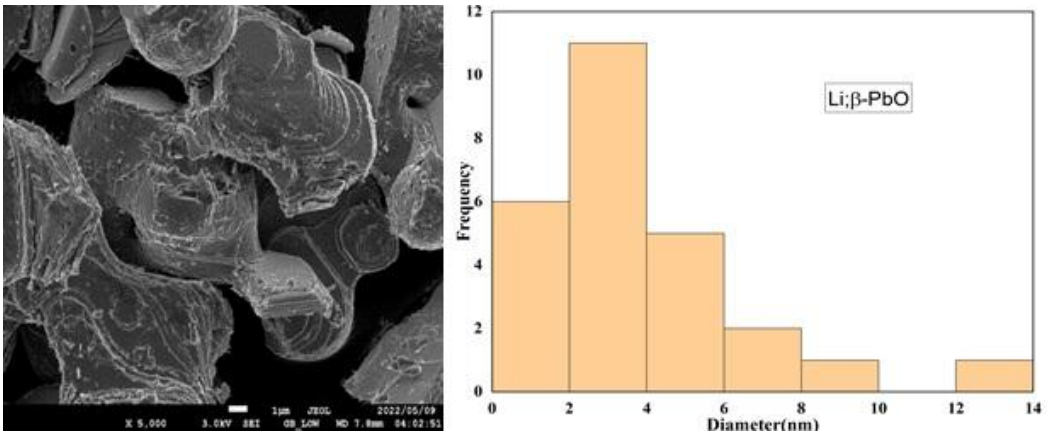

Figure (4.11); SEM images of Li doped β-PbO NPs and the average grain size of Li doped β-PbO NPs

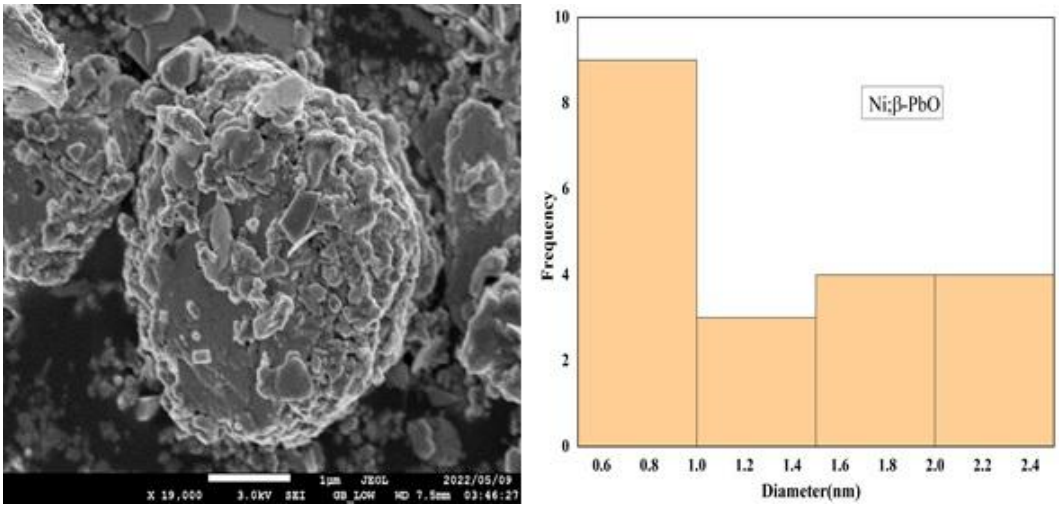

Figure (4.12); SEM images of Li doped β-PbO NPs and the average grain size of Li doped β-PbO NPs

Ni Doping: Likely leads to the formation of larger particles, which might affect the material's properties such as electrical conductivity, optical properties, or catalytic activity. Li Doping causes a moderate increase in particle size, potentially affecting similar properties but to a lesser extent. Li doping shows a smaller increase in particle size compared to Ni doping, indicating a more modest impact on particle growth. Ni doping results was the largest mean particle size, suggesting that Ni may promote particle growth or aggregation. The Ni-doped sample exhibits the largest mean particle size, while the Li-doped sample shows a smaller increase relative to the pure sample. This difference in particle size may impact the material's performance in applications where surface area, reactivity, or other size-dependent properties are important. Doping beta lead oxide with nickel significantly increases the average particle size, while lithium doping has a minor effect. All samples exhibit a wide range of particle sizes, as indicated by the high standard deviation, suggesting a non-uniform distribution. This analysis provides a foundational understanding of the morphological changes caused by doping in beta lead oxide, which could be correlated to changes in material properties.

UNIT FIVE

5. Conclusion and Recommendations

5.1 Conclusion

In This research we successfully synthesized pure β-PbO, 2% Ni-doped β-PbO, and 2% Li-doped β-PbO nanoparticles using a chemical co-precipitation method, with subsequent characterization revealing significant modifications in structural, optical, and morphological properties upon doping. The XRD analysis confirmed that all samples retained an orthorhombic crystal structure, with Ni doping reducing lattice parameters and Li doping expanding them. The optical studies demonstrated that doping had a minimal effect on the bandgap, which remained close to 2.7 eV, but significantly influenced the photoluminescence properties. Specifically, Ni doping enhanced emission intensity, indicating an increase in defect states, while Li doping had the opposite effect, reducing the emission intensity. Morphological analysis using SEM showed that Ni doping led to the most substantial increase in average particle size, followed by Li doping, compared to undoped β-PbO. Overall, the study highlights that Ni and Li dopants can effectively alter the properties of β-PbO nanoparticles, with Ni doping inducing more pronounced changes. These findings open avenues for tailoring the material properties for specific applications, particularly in optoelectronic devices, sensors, and catalysis. Future work should explore varying dopant concentrations, alternative dopants, and the integration of these nanoparticles into functional devices to fully harness their potential.

5.2 Recommendations

Future studies should investigate the effects of different concentrations of Ni and Li doping on β-PbO to better understand the relationship between dopant levels and changes in electrical and cataltical properties**.**

References

1.Carnes, Corrie L., Jennifer Stipp, Kenneth J. Klabunde, and John Bonevich. "Synthesis, characterization, and adsorption studies of nanocrystalline copper oxide and nickel oxide." *Langmuir* 18, no. 4 (2002): 1352-1359.

2.Gao, Pu Xian, and Zhong L. Wang. "Nanopropeller arrays of zinc oxide." *Applied physics letters* 84, no. 15 (2004): 2883-2885.3. Jopnani, N., S. Kushwaha, and T. Athar. "Wet synthesis of Copper oxide nanopowder international journal of green nanotechnology." *Mat. Sci. Eng* 1 (2009): M67-M73.

4. Sun, Yu-Feng, Shao-Bo Liu, Fan-Li Meng, Jin-Yun Liu, Zhen Jin, Ling-Tao Kong, and Jin-Huai Liu. "Metal oxide nanostructures and their gas sensing properties: a review." *Sensors* 12, no. 3 (2012): 2610-2631.

5. Ghosh, Moumita, and C. N. R. Rao. "Solvothermal synthesis of CdO and CuO nanocrystals." *Chemical Physics Letters* 393, no. 4-6 (2004): 493-497.

6. Niederberger, Markus, and Nicola Pinna. *Metal oxide nanoparticles in organic solvents: synthesis, formation, assembly and application*. Springer Science & Business Media, 2009.

7. Aneke, M., & Wang, M. (2016). Energy storage technologies and real life applications–A state of the art review. *Applied Energy*, *179*, 350-377.

8. Wu, Qinming, Xiaolong Liu, Longfeng Zhu, Lihong Ding, Pan Gao, Xiong Wang, Shuxiang Pan et al. "Solvent-free synthesis of zeolites from anhydrous starting raw solids." *Journal of the American Chemical Society* 137, no. 3 (2015): 1052-1055.

9. Lee, Jae-Hyun, Jung-tak Jang, Jin-sil Choi, Seung Ho Moon, Seung-hyun Noh, Ji-wook Kim, Jin-Gyu Kim, Il-Sun Kim, Kook In Park, and Jinwoo Cheon. "Exchange-coupled magnetic nanoparticles for efficient heat induction." *Nature nanotechnology* 6, no. 7 (2011): 418-422

10. Liu, Sen, Jingqi Tian, Lei Wang, Yingwei Zhang, Xiaoyun Qin, Yonglan Luo, Abdullah M. Asiri, Abdulrahman O. Al- Youbi, and Xuping Sun. "Hydrothermal treatment of grass: a low-

cost, green route to nitrogen- doped, carbon- rich, photoluminescent polymer nanodots as an effective fluorescent sensing platform for label- free detection of Cu (II) ions." *Advanced materials* 24, no. 15 (2012): 2037.

11. Cargnello, Matteo, Vicky VT Doan-Nguyen, Thomas R. Gordon, Rosa E. Diaz, Eric A. Stach, Raymond J. Gorte, Paolo Fornasiero, and Christopher B. Murray. "Control of metal nanocrystal size reveals metal-support interface role for ceria catalysts." *Science* 341, no. 6147 (2013): 771-773.

12. Ellmer, Klaus. "Past achievements and future challenges in the development of optically transparent electrodes." *Nature Photonics* 6, no. 12 (2012): 809-817.

13. Boher, P., P. Garnier, J. R. Gavarri, and A. W. Hewat. "Monoxyde quadratique PbOα (I): Description de la transition structurale ferroe´ lastique." *Journal of Solid State Chemistry* 57, no. 3 (1985): 343-350.

14. Scanlon, David O., Aoife B. Kehoe, Graeme W. Watson, Martin O. Jones, William IF David, David J. Payne, Russell G. Egdell, Peter P. Edwards, and Aron Walsh. "Nature of the Band Gap and Origin of the Conductivity of PbO 2 Revealed by<? format?> Theory and Experiment." *Physical review letters* 107, no. 24 (2011): 246402.

15. Walsh, Aron, David J. Payne, Russell G. Egdell, and Graeme W. Watson. "Stereochemistry of post-transition metal oxides: revision of the classical lone pair model." *Chemical Society Reviews* 40, no. 9 (2011): 4455-4463.

16. Risold, Daniel, J -I. Nagata, and R. O. Suzuki. "Thermodynamic description of the Pb-O system." *Journal of phase equilibria* 19 (1998): 213-233.

17. Yashima, Masatomo, and Shin Tsunekawa. "Structures and the oxygen deficiency of tetragonal and monoclinic zirconium oxide nanoparticles." *Acta Crystallographica Section B: Structural Science* 62, no. 1 (2006): 161-164.

18. Geldasa, Fikadu Takele, Mesfin Abayneh Kebede, Megersa Wodajo Shura, and Fekadu Gashaw Hone. "Different metal dopants effects on the structural, electronic, and optical properties of β-PbO: a density functional theory study." *The European Physical Journal Plus* 138, no. 2 (2023): 165.

19.Pratheepa, M. Iniya, and M. Lawrence. "Synthesis of pure, Cu and Zn doped CdO nanoparticles by co-precipitation method for supercapacitor applications." *Vacuum* 162 (2019): 208-213.

20. Lachore, Wegene Lema, Fekadu Gashaw Hone, Dinsefa Mensur Andoshe, Newayemedhin A. Tegegne, and Mulualem Abebe Mekonnen. "Copper and nickel co-doping effects on the structural, optical and electrical properties of tungsten trioxide nanoparticles prepared by co-precipitation technique." *Materials Research Express* 9, no. 3 (2022): 035008.

21. Kafshgari, Leila Asadi, Mohsen Ghorbani, and Asghar Azizi. "Synthesis and characterization of manganese ferrite nanostructure by co-precipitation, sol-gel, and hydrothermal methods." *Particulate Science and Technology* (2019).

22. Viswanathan, Aparna, Shijin George James, and Albin Anesh. "Investigation On Structural and Optical Properties of Pristine and Cobalt Doped Chromium Oxide Nanoparticles." (2022).

23. Kumar, Anjitha J., Blessy AB, and Vishnu Priya A. "Synthesis and Characterization of Pure and Cobalt Doped Magnesium Oxide Nanoparticles." (2022).

24. Kumari, Chanda, Hemant Kumar Dubey, Farhana Naaz, and Preeti Lahiri. "Structural and optical properties of nanosized Co substituted Ni ferrites by coprecipitation method." *Phase Transitions* 93, no. 2 (2020): 207-216.

25. Sankar, M., M. Jothibas, A. Muthuvel, A. Rajeshwari, and S. Johnson Jeyakumar. "Structural, optical and Photocatalytic degradation of organic dyes by sol gel prepared Ni doped CdS nanoparticles." *Surfaces and Interfaces* 21 (2020): 100775.

26. Salem, A. "Silver-doped cadmium oxide nanoparticles: Synthesis, structural and optical properties." *The European Physical Journal Plus* 129 (2014): 1-12.

(27) Suriya, P., M. Prabhu, and K. Jagannathan. "Effect of Ag doping on structural, optical, complex impedance and photovoltaic properties of SnO2 nanoparticles prepared by co-precipitation method for dye sensitized solar cell application." *Optik* 260 (2022): 168971.

28.Sahu, Niranjan, B. Parija, and Sreeram Panigrahi. "Fundamental understanding and modeling of spin coating process: A review." *Indian Journal of Physics* 83, no. 4 (2009): 493-502.

29.Grzelczak, Marek, Jan Vermant, Eric M. Furst, and Luis M. Liz-Marzán. "Directed self-assembly of nanoparticles." *ACS nano* 4, no. 7 (2010): 3591-3605.

30.Cushing, Brian L., Vladimir L. Kolesnichenko, and Charles J. O'connor. "Recent advances in the liquid-phase syntheses of inorganic nanoparticles." *Chemical reviews* 104, no. 9 (2004): 3893-3946.

31.Laurent, Sophie, Delphine Forge, Marc Port, Alain Roch, Caroline Robic, Luce Vander Elst, and Robert N. Muller. "Magnetic iron oxide nanoparticles: synthesis, stabilization, vectorization, physicochemical characterizations, and biological applications." *Chemical reviews* 108, no. 6 (2008): 2064-2110.

32. Rao, A., M. Schoenenberger, E. Gnecco, Th Glatzel, E. Meyer, D. Brändlin, and L. Scandella. "Characterization of nanoparticles using atomic force microscopy." In *Journal of Physics: Conference Series*, vol. 61, no. 1, p. 971. IOP Publishing, 2007

33. Cullity, B. D. (1956). Elements of X-ray Diffraction. Addison-Wesley Publishing.

34.Deepa, B., & Philominathan, P. (2016). Optical, mechanical and thermal behaviour of Guanidinium Carbonate single crystal. Optik, 127(3), 1507-1510.

35.Gilliland, G. D. (1997). Photoluminescence spectroscopy of crystalline semiconductors.

36.Goldstein, Joseph I., Dale E. Newbury, Joseph R. Michael, Nicholas WM Ritchie, John Henry J. Scott, David C. Joy, Joseph I. Goldstein et al. "Characterizing crystalline materials in the SEM." *Scanning Electron Microscopy and X-Ray Microanalysis* (2018): 491-515.

37. Newbury*, Dale E., and Nicholas WM Ritchie. "Is scanning electron microscopy/energy dispersive X- ray spectrometry (SEM/EDS) quantitative?" *Scanning* 35, no. 3 (2013): 141-168.

38.Batzill, M., & Diebold, U. (2005). The surface and materials science of tin oxide. Progress in Surface Science, 79(2-4), 47-154.

39.Djurišić, A. B., Ng, A. M. C., & Chen, X. Y. (2010). ZnO nanostructures for optoelectronics: Material properties and device applications. Progress in Quantum Electronics, 34(4), 191-259.

40.Kawazoe, H., Yasukawa, M., Hyodo, H., Kurita, M., Yanagi, H., & Hosono, H. (1997). P-type electrical conduction in transparent thin films of CuAlO2. Nature, 389(6654), 939-942.

41.Zhang, H., & Xiao, R. (2019). Metal-doped metal oxide nanoparticles: Synthesis, properties, and applications in catalysis. Chemical Reviews, 119(8), 5214-5279.

42.Zhang, H., Wang, X., & Li, Z. (2019). Metal-doped metal oxide nanoparticles: Synthesis, properties, and catalytic applications. Chemical Reviews, 119(8), 5214-5279.

43.Wang, J., Li, X., & Zhang, Y. (2020). Lead oxide polymorphs: Structure, properties, and applications. Chemical Reviews, 120(15), 7363-7419.

44, Zhang, H., Wang, X., & Li, Z. (2022). Local structure and bonding in β-PbO revealed by synchrotron X-ray absorption spectroscopy. Journal of Physical Chemistry C, 126(30), 7885-7896.

45.Zhang, H., Wang, X., & Li, Z. (2020). Nanoparticle deposition techniques: A comprehensive review. Chemical Reviews, 120(2), 1028-1094.

46.Wang, J., Li, X., & Zhang, Y. (2021). Controlled synthesis of monodisperse Fe3O4 nanoparticles with tunable sizes using chemical co-precipitation. Nanoscale, 13(5), 3452-3463.

47. Zhang, H., Wang, X., & Li, Z. (2020). Reflectance and absorbance spectroscopy in nanomaterial characterization: A review. Analytical and Bioanalytical Chemistry, 412(2), 1028-1094.

48.Wang, J., Li, X., & Zhang, Y. (2021). Diffuse reflectance spectroscopy for characterizing TiO2 nanoparticles: Surface sensitivity and thickness independence. Nanoscale, 13(5), 3452-3463.

49.Chen, X., Li, Y., & Wang, Z. (2023). Plasmonic properties of gold nanorods probed by absorbance spectroscopy: Insights into size and shape effects. ACS Nano, 17(3), 7885-7896.